Statistical Modeling of THz Scatter Channels

Seunghwan Kim and Alenka Zajić
School of Electrical and Computer Engineering
Georgia Institute of Technology, Atlanta, GA 30332 USA

***Abstract*— A two-dimensional (2-D) geometrical propagation model for wideband terahertz (THz) indoor communications is proposed. Based on the geometrical model, a parametric reference model for wideband THz multipath fading channels is developed. From the reference model, the corresponding power delay profile is derived and compared with measured data. The results show good agreement between measured and simulated power delay spectra.**

I. Introduction

Ultra-wideband Terahertz (THz) communication systems are expected to help satisfy the ever-growing need for higher speed wireless communication anywhere and anytime. The terahertz (THz) range spans frequencies between 300 GHz and 10 THz and offers very large unregulated bandwidths in excess of 10 GHz [1], [2]. This large bandwidth paired with higher speed wireless links can open the door to a large number of novel applications such as ultra-high-speed pico-cell cellular links, wireless short-range communications, secure wireless communication for military and defense applications, and on-body communication for health monitoring systems.

To successfully design THz communication systems, it is necessary to have a detailed knowledge of the THz indoor multipath fading channel and its statistical properties. The first THz free-space measurements at lower end of THz range (300 GHz with bandwidth of 10 GHz) have been reported in [3]-[5] for two indoor scenarios: 1) a free-space link of devices on a desktop and 2) a free-space connection of a laptop to an access point in the middle of an office. Recently, THz free-space measurements and statistical characterization of 300 GHz channel with bandwidth of 20 GHz have been reported in [6], [7] for a free-space link of devices on a desktop. The first ray-tracing and path-loss models for THz communications have been reported in [8]-[13]. However, no statistical channel models for THz indoor multipath fading channels have been proposed.

To address this problem, this paper introduces a new 2-D reference model for *THz* wideband indoor channels and shows that this model can match the measured data in indoor environments. Here, we consider point-to-point communication links between two stationary directional antennas. From the scattering point of view, the THz indoor channels have similar scattering patterns as other indoor (GHz or $\mathrm{mm-wave}$) channels. However, in addition to that, THz signals may get reflected from the objects behind the receive ($\mathrm{R_x}$) antenna, travel back to the objects near the transmit ($\mathrm{T_x}$) antenna and reflect back to be received by the $\mathrm{R_x}$ antenna. This effect has been observed in two independent measurement campaigns [3], [7] and is the consequence of using very directional and high gain antennas. While these reflections can be suppressed in channel sounding experiments by putting absorbers around the $\mathrm{T_x}$ and $\mathrm{R_x}$, in practice channel models and communication systems need to account for them.

In this paper, we propose a 2-D model for wideband THz channels that accounts for line-of-sight (LoS), single-reflection (SR) rays, and double-reflection (DR) rays. To describe our 2-D reference model, we first introduce a 2-D geometrical model for wideband THz channels that consists of concentric sectors filled with scatterers around the $\mathrm{T_x}$ and $\mathrm{R_x}$. This model is chosen to adequately account for directionality of the antennas, one of the key features in THz channels. Then, we propose a parametric reference model that employs the concentric-sectors geometry and constructs the input delay-spread function as a superposition of LoS, SR, and DR rays. The parametric nature of the model makes it adaptable to a variety of propagation environments, i.e., free-space, desktop, chip-to-chip, or indoor environments. From the new reference model, we derive the corresponding power delay profile (PDP) for a 2-D isotropic scattering environment. Finally, we compare the PDPs with those obtained from measurements in [7] to illustrate the importance of combining the LoS, SR, and DR rays.

The remainder of the paper is organized as follows. Section II introduces the geometrical concentric-sectors model and presents a 2-D reference model for wideband THz indoor channels. Section III derives PDP for a 2-D isotropic scattering environment. Section IV compares measured and simulated power delay spectra. Finally, Section V provides some concluding remarks.

II. A Reference Model for Wideband THz Channels

This paper considers a wide-band THz indoor communication link between the stationary $\mathrm{T_x}$ and $\mathrm{R_x}$. It is assumed that both the $\mathrm{T_x}$ and $\mathrm{R_x}$ are equipped with directional antennas. This is typical assumption for THz channels due to high path loss. The radio propagation in indoor environments is characterized by 2-D wide sense stationary uncorrelated scattering (WSSUS) with either LoS or NLoS conditions between the $\mathrm{T_x}$ and $\mathrm{R_x}$.

Fig. 1 shows the concentric-sectors model with LoS, SR, and DR rays. Concentric-sectors are chosen to include antenna directionality into the model. The concentric-sectors model defines four arcs, two around the $\mathrm{T_x}$ and another two around the $\mathrm{R_x}$, as shown in Fig. 1. It is assumed that M fixed

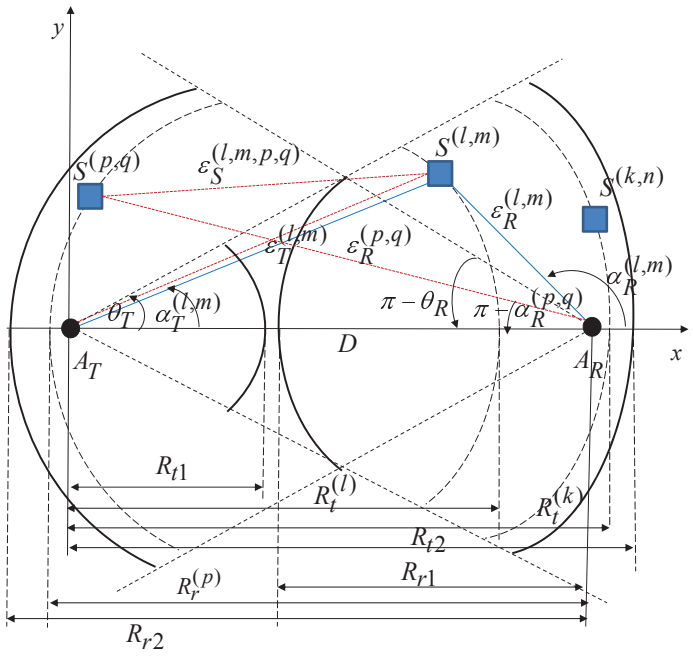

Fig. 1. The concentric-sectors model with LoS , SR, and DR rays for a wideband THz indoor channel.

omnidirectional scatterers occupy an area between sectors of radii R_{t1} and R_{t2}. The lower-boundary on the $\mathrm{R_x}$ sector area is set in the far-field region of the $\mathrm{T_x}$ antenna such that scatterers do not fully block the propagation path. The upper-boundary on the $\mathrm{R_x}$ sector area is set behind the $\mathrm{R_x}$. It is assumed that the M scatterers lie on L arcs of radii $R_{t1} \leq R_t^{(l)} \leq R_{t2}$, where $1 \leq l \leq L$. To account for clustering effect, the l^{th} arc contains $M^{(l)}$ fixed omnidirectional scatterers, and the $(m,l)^{th}$ scatterer is denoted by $S^{(m,l)}$, where $1 \leq m \leq M^{(l)}$. Similarly, around the transmitter, Q fixed omnidirectional scatterers occupy an area between sectors of radii R_{r1} and R_{r2}. The lower-boundary on the $\mathrm{T_x}$ sector area is set at the intersection of the $\mathrm{T_x}$ and $\mathrm{R_x}$ antenna beam-width angles (θ_T and θ_R) and the upper-boundary on the $\mathrm{T_x}$ sector area is set behind the $\mathrm{T_x}$. It is assumed that the Q scatterers lie on P arcs of radii $R_{r1} \leq R_r^{(p)} \leq R_{r2}$, where $1 \leq p \leq P$. The p^{th} arcs contains $Q^{(p)}$ fixed omnidirectional scatterers, and the $(p,q)^{th}$ receive scatterer is denoted by $S^{(p,q)}$, where $1 \leq q \leq Q^{(p)}$. The distance between the centers of the $\mathrm{T_x}$ and $\mathrm{R_x}$ is D. The symbols $\epsilon_T^{(m,l)}$, $\epsilon_R^{(m,l)}$, $\epsilon_S^{(l,m,p,q)}$, and $\epsilon_R^{(p,q)}$ denote distances A_T - $S^{(m,l)}$, $S^{(m,l)}$ - A_R, $S^{(m,l)}$ - $S^{(p,q)}$, and $S^{(p,q)}$ - A_R respectively, as shown in Fig. 1. Angles θ_T and θ_R in Fig. 1 describe the half-beamwidth of the $\mathrm{T_x}$ and $\mathrm{R_x}$ antenna in the x - y plane, respectively, relative to the x - axis. The symbol $\alpha_T^{(m,l)}$ denotes the angles of departure (AoD) of the waves that impinge on the scatterers $S^{(m,l)}$, whereas $\alpha_R^{(p,q)}$ denotes the angles of arrivals (AoA) of the waves double-scattered from $S^{(m,l)}$ and $S^{(p,q)}$.

Observe from the 2-D geometrical model in Fig. 1 that some waves from the $\mathrm{T_x}$ antenna elements may traverse directly to the $\mathrm{R_x}$ antenna elements (LoS rays), while others are single-reflected in the $\mathrm{R_x}$ sector area (i.e., the waves from the $\mathrm{T_x}$ antenna elements scatter from the scatterers $S^{(m,l)}$ in the $\mathrm{R_x}$ sector area before arriving at the $\mathrm{R_x}$ antenna elements), and/or double-reflected (i.e., the waves from the $\mathrm{T_x}$ antenna elements impinge on the scatterers $S^{(m,l)}$ in the $\mathrm{R_x}$ sector area and scatter from the scatterers $S^{(p,q)}$ in the $\mathrm{T_x}$ sector area before arriving at the $\mathrm{R_x}$ antenna elements). Hence, the time-invariant input delay-spread function of the link A_T - A_R can be written as a superposition of the LoS, SR, and DR rays, viz.

$$h(\tau) \;=\; h^{SR}(\tau) + h^{DR}(\tau) + h^{LoS}(\tau). \tag{1}$$

The single-reflected component of the input delay-spread function is

$$h^{SR}(\tau) = \sqrt{\frac{\eta_{SR}}{K+1}} \frac{1}{\sqrt{M}} \sum_{l=1}^{L} \sum_{m=1}^{M^{(l)}} A_{m,l} e^{j\phi_{m,l}} \delta(\tau - \tau_{m,l}), \tag{2}$$

where $A_{m,l}$ is the amplitude, $\phi_{m,l}$ is the phase, $\tau_{m,l}$ is the time delay of the multipath components, and K is the Rice factor (ratio of LoS to scatter received power). The amplitudes of the multipath components $A_{m,l}$ are defined as

$$A_{m,l} = \frac{\lambda \sqrt{G_T \cdot G_R}}{4\pi \left[\epsilon_T^{(m,l)} + \epsilon_R^{(m,l)}\right]^{\gamma/2}}, \tag{3}$$

where G_T and G_R are the $\mathrm{T_x}$ and $\mathrm{R_x}$ antenna gains, respectively, and γ is the path loss exponent. The time delays $\tau_{m,l}$ are the travel times of the waves scattered from the scatterers $S^{(m,l)}$, i.e.,

$$\tau_{m,l} \;=\; \frac{\epsilon_T^{(m,l)} + \epsilon_R^{(m,l)}}{c_0} \tag{4}$$

where c_0 is the speed of light.

The double-bounced component of the input delay-spread function is

$$h^{DR}(\tau) = \sqrt{\frac{\eta_{DR}}{K+1}} \tag{5}$$
$$\frac{1}{\sqrt{MQ}} \sum_{l,m=1}^{L,M^{(l)}} \sum_{p,q=1}^{P,Q^{(p)}} A_{m,l,p,q} e^{\phi_{m,l,p,q}} \delta(\tau - \tau_{m,l,p,q}),$$

where $A_{m,l,p,q}$, $\phi_{m,l,p,q}$ and $\tau_{m,l,p,q}$ denote the amplitudes, phases, and time delays of the multipath components, respectively. The amplitude of the multipath component $A_{m,l,p,q}$ is defined as

$$A_{m,l,p,q} = \frac{\lambda \sqrt{G_T \cdot G_R}}{4\pi \left[\epsilon_T^{(m,l)} + \epsilon_S^{(l,m,p,q)} + \epsilon_R^{(p,q)}\right]^{\gamma/2}}. \tag{6}$$

Finally, the time delay $\tau_{m,l,p,q}$ is the travel time of the wave impinged on the scatterer $S^{(m,l)}$ and scattered from the scatterer $S^{(p,q)}$, i.e.,

$$\tau_{m,l,p,q} \;=\; \frac{\epsilon_T^{(m,l)} + \epsilon_S^{(l,m,p,q)} + \epsilon_R^{(p,q)}}{c_0}. \tag{7}$$

The parameters η_{SR} and η_{DR} in (2) and (5), respectively, specify how much the single- and double-reflected rays contribute in the total power, i.e., these parameters satisfy $\eta_{SR}+\eta_{DR}=1$. It is assumed that the angles of departure ($\alpha_T^{(m,l)}$) and the angles of arrival ($\alpha_R^{(p,q)}$) are random variables. Furthermore, it is assumed that the radii $R_t^{(l)}$ and $R_r^{(p)}$ are independent random variables. Finally, it is assumed that the phases $\phi_{m,l}$, $\phi_{p,q}$, and $\phi_{m,l,p,q}$ are uniform random variables on the interval $[-\pi,\pi)$ that are independent from the angles of departure, the angles of arrival, and the radii of the sectors. Using the assumptions introduced above and the Central Limit Theorem, we can conclude that $h^{SR}(\tau)$ and $h^{DR}(\tau)$ are independent zero-mean complex Gaussian random processes. Furthermore, note that double-reflected rays have the angles of departure $\alpha_T^{(m,l)}$ independent from the angles of arrival $\alpha_R^{(p,q)}$ [14]. On the other hand, single-reflected rays have angles of arrival $\alpha_R^{(m,l)}$ that are dependent on the angles of departure $\alpha_T^{(m,l)}$ and angles of departure $\alpha_T^{(p,q)}$ that are dependent on the angles of arrival $\alpha_R^{(p,q)}$. Using small angle approximation $\sin x \approx x$ for small x, it can be shown that $\alpha_T^{(p,q)} \approx \alpha_R^{(p,q)}/(1+D/R_r^{(p)})$, and $\alpha_R^{(m,l)} \approx \alpha_T^{(m,l)}/(1-D/R_t^{(l)})$.

The LoS component of the input delay-spread function is

$$h^{LoS}(\tau) = \sqrt{\frac{K}{K+1}} A_{LoS} e^{j\phi_{LoS}} \delta(\tau-\tau_{LoS}), \tag{8}$$

where the LoS amplitude is $A_{LoS}=\sqrt{G_T G_R}\lambda/(4\pi D^{\gamma/2})$, the LoS time delay is $\tau_{LoS}=D/c_0$, and the LoS phase is ϕ_{LoS}.

Finally, we observe that the distances $\epsilon_T^{(m,l)}$, $\epsilon_R^{(m,l)}$, $\epsilon_S^{(l,m,p,q)}$, and $\epsilon_R^{(p,q)}$ can be expressed as functions of the random variables $\alpha_T^{(m,l)}$, $\alpha_R^{(p,q)}$, $R_t^{(l)}$, and $R_r^{(p)}$ as follows:

$$\epsilon_T^{(m,l)} = R_t^{(l)} \tag{9}$$

$$\epsilon_R^{(m,l)} = D\sin\alpha_T^{(m,l)} \times \sqrt{1+\frac{\left(R_t^{(l)}-D\cos\alpha_T^{(m,l)}\right)^2}{\left(D\sin\alpha_T^{(m,l)}\right)^2}}, \tag{10}$$

$$\epsilon_S^{(l,m,p,q)} = R_t^{(l)}\cos\alpha_T^{(m,l)} + R_t^{(l)}\sin\alpha_T^{(m,l)} \times \cot(\pi-(\alpha_R^{(p,q)}/(1+D/R_r^{(p)}))), \tag{11}$$

$$\epsilon_R^{(p,q)} = R_r^{(p)}. \tag{12}$$

Since all locations of scatterers in indoor environment are equally probable, we assume uniformly distributed scattering in the concentric-sectors model and to characterize it we use the joint probability density function (pdf)

$$f(R,\alpha) = \frac{2R}{(\alpha_2-\alpha_1)(R_2^2-R_1^2)}. \tag{13}$$

Since it can be shown that $f(R,\alpha)=f(R)\cdot f(\alpha)$, it implies that the radii and the angles of arrival and departure are independent random variables. Hence, the radii $R_t^{(l)}$ and $R_r^{(p)}$ are uniformly distributed between R_{t1} and R_{t2} and R_{r1} and R_{r2}, respectively. Similarly, the AoDs $\alpha_T^{(m,l)}$ and the AoAs $\alpha_R^{(p,q)}$ are uniformly distributed between $(2\pi-\theta_T)$–θ_T and $(\pi-\theta_R)$–$(\pi+\theta_R)$, respectively. Such a distribution implies that the scatterers in the horizontal plane will have a uniform density between the concentric-sectors, if the scattering is isotropic in the horizontal plane.

III. Power Delay Profile of the Reference Model

In time-invariant channels, the power delay profile (PDP) is defined as the envelope of $h(\tau)$ [14], i.e.,

$$P(\tau) = |h(\tau)|^2. \tag{14}$$

Since $h^{SR}(\tau)$ and $h^{DR}(\tau)$ are independent zero-mean complex Gaussian random processes, it follows that the PDP is a summation of the PDP functions of the SR, DR, and LoS components and can be written as:

$$P(\tau) = P^{SR}(\tau)+P^{DR}(\tau)+P^{LoS}(\tau). \tag{15}$$

The single-reflected component of the PDP is

$$P^{SR}(\tau) = \frac{\eta_{SR}}{K+1}\frac{1}{M}\sum_{l=1}^{L}\sum_{m=1}^{M^{(l)}} A_{m,l}^2\delta(\tau-\tau_{m,l}) = \frac{\eta_{SR}}{K+1}\frac{1}{M}\sum_{l=1}^{L}\sum_{m=1}^{M^{(l)}} \frac{\lambda^2 G_T\cdot G_R}{(4\pi)^2\left[\epsilon_T^{(m,l)}+\epsilon_R^{(m,l)}\right]^{\gamma}} \times \delta\left[\tau-\frac{\epsilon_T^{(m,l)}+\epsilon_R^{(m,l)}}{c}\right]. \tag{16}$$

The double-reflected component of the PDP is

$$P^{DR}(\tau) = \frac{\eta_{DR}}{K+1}\frac{1}{MQ}\sum_{l,m=1}^{L,M^{(l)}}\sum_{p,q=1}^{P,Q^{(p)}} A_{m,l,p,q}^2 \times \delta(\tau-\tau_{m,l,p,q}) = \frac{\eta_{DR}}{K+1}\frac{1}{MQ}\sum_{l,m=1}^{L,M^{(l)}}\sum_{p,q=1}^{P,Q^{(p)}} \times \frac{\lambda^2 G_T\cdot G_R}{(4\pi)^2\left[\epsilon_T^{(m,l)}+\epsilon_S^{(l,m,p,q)}+\epsilon_R^{(p,q)}\right]^{\gamma}} \times \delta(\tau-\frac{\epsilon_T^{(m,l)}+\epsilon_S^{(l,m,p,q)}+\epsilon_R^{(p,q)}}{c}). \tag{17}$$

Finally, the LoS component of the PDP is

$$P^{LoS}(\tau) = \frac{K}{K+1}A_{LoS}^2\delta(\tau-\tau_{LoS}) = \frac{K}{K+1}\frac{G_T G_R(\lambda)^2}{(4\pi)^2 D^{\gamma}}\delta(\tau-D/c). \tag{18}$$

Fig. 2 plots several PDPs that can be found in THz indoor channels. We assume WSSUS isovelocity scattering environment with the carrier frequency $f_c = 300$ GHz. Furthermore, we choose the distance between the $\mathrm{T_x}$ and $\mathrm{R_x}$ to be $D = 20$ cm. The $\mathrm{T_x}$ and $\mathrm{R_x}$ have antenna beamwidths $2\theta_T = 2\theta_R = 10^\circ$. The LoS propagation scenario is assumed with Ricean factor $K = 2$, the number of scatterers is set to $L = P = 10$, $M = Q = 50$, and the radii are

chosen to be $R_{t1} = 0.1$ m, $R_{t2} = 0.25$ m, $R_{r1} = 0.1$ m, $R_{r2} = 0$ m, respectively. To illustrate the impact of the single-reflected and double-reflected rays, we vary η_{SR} from 0 to 1. From Fig. 2, we can observe that when single-reflected rays are dominant, i.e., when $\eta_{SR} = 1$, the excess delay time is much shorter then when double-reflected rays are dominant, i.e., when $\eta_{DR} = 1$. Also, we can observe that when both single-reflected and double-reflected rays are equally present, i.e., $\eta_{SR} = \eta_{DR} = 0.5$, the amplitudes of the reflections are lower, because single- and double-reflected rays constructively or destructively combine.

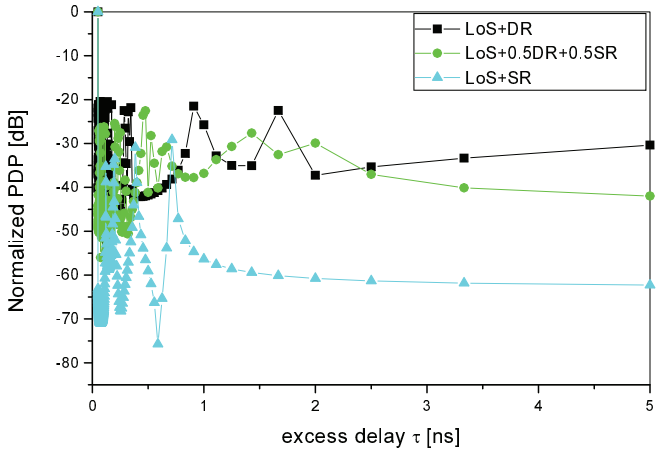

Fig. 2. The normalized theoretical PDP with the distance between the $\mathrm{T_x}$ and $\mathrm{R_x}$ $D = 20$ cm in several THz indoor scenarios.

IV. Comparison with Measured Data

In this section, we compare the theoretical results in Section III with the measured PDP data in [7].

The channel measurements in [7] are collected at $f_c = 300$ GHz with bandwidth of 20 GHz. The distance between the $\mathrm{T_x}$ and $\mathrm{R_x}$ was varied between 10 cm and 40 cm. The $\mathrm{T_x}$ and $\mathrm{R_x}$ are equipped with directional horn antennas with equal beam-widths (i.e., $2\theta_T = 2\theta_R = 10°$). It is assumed that the $\mathrm{T_x}$ and $\mathrm{R_x}$ are stationary, positioned on a desktop and free of local scatterers. The measurements show that the measured PDP consists of the LoS component and the double-reflected component.

Figs. 3 and 4 compare the simulated and measured PDP functions for two distances $D = 20$ cm and $D = 40$ cm, respectively. The analytical PDP in Fig. 3 is obtained with the parameters $K = 1.9$, $L = P = 10$, $M = Q = 50$, $R_{t1} = 0.1$ m, $R_{t2} = 0.25$ m, $R_{r1} = 0.1$ m, $R_{r2} = 0$ m, $\eta_{SR} = 0$, and $\eta_{DR} = 1$. The Rice factor K is estimated from the measurements, η_{DR} is set to 1 because there are no single-reflections in the measurements, and the rest of the parameters are estimated jointly using the maximum-likelihood approach in [14]. Similarly, the analytical PDP in Fig. 4 is obtained with the parameters $K = 1.9$, $L = P = 10$, $M = Q = 50$, $R_{t1} = 0.2$ m, $R_{t2} = 0.45$ m, $R_{r1} = 0.2$ m, $R_{r2} = 0$ m, $\eta_{SR} = 0$, and $\eta_{DR} = 1$.

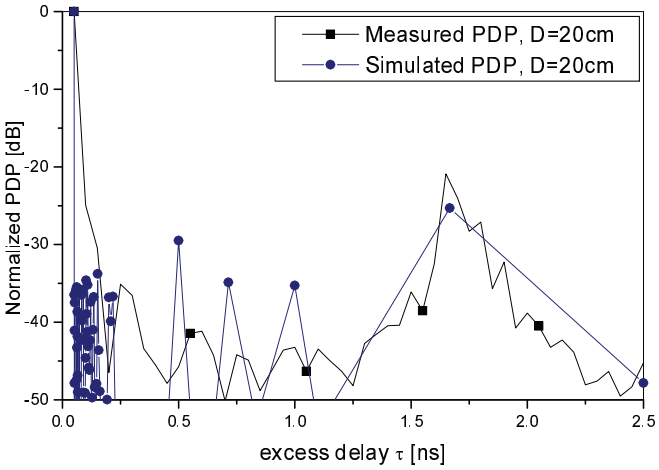

Fig. 3. The normalized theoretical and measured PDP with the distance between the $\mathrm{T_x}$ and $\mathrm{R_x}$ $D = 20$ cm.

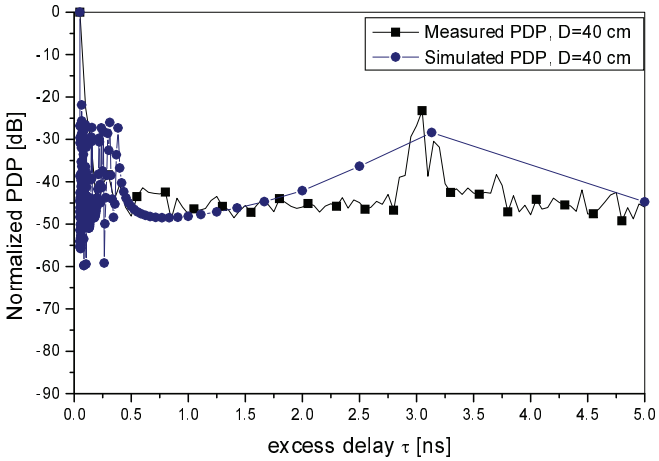

Fig. 4. The normalized theoretical and measured PDP with the distance between the $\mathrm{T_x}$ and $\mathrm{R_x}$ $D = 40$ cm.

The results show that the simulated PDPs follow well the shape of the measured PDPs. The discrepancies between the measured and simulated PDPs for short delay excesses are due to different time scale resolutions. All multipaths arriving with short time delays are lumped together in the measurements, while in the simulations each arriving multipath is captured individually. Also, we can observe that measured PDP sometimes has lower amplitude than predicted by the model. This discrepancy is because our model assumes lossles reflections, which is not a realistic assumption, but significantly simplifies modeling.

V. Conclusions

A two-dimensional geometrical propagation model for wideband terahertz (THz) indoor communications was proposed. Based on the geometrical model, a parametric reference model for wideband THz multipath fading channels was developed. From the reference model, the corresponding power delay profiles were derived and compared with measured

data. The results show good agreement between measured and simulated PDPs.

REFERENCES

[1] S. Cherry,"Edholm's law of bandwidth," *IEEE Spectrum*, vol. 41, pp. 58–60, July 2004.

[2] P. H. Siegel,"Terahertz technology," *IEEE Transactions on Microwave Theory and Techniques*, MTT-50, pp. 910–928, March 2002.

[3] S. Priebe, C. Jastrow, M. Jacob, T. Kleine-Ostmann, T. Schrader, T. Kürner, "Channel and propagation measurements at 300 GHz," *IEEE Transactions on Antennas and Propagation*, vol. 59, no. 5, pp. 1688–1698, May 2011.

[4] R. Piesiewicz, T. Kleine-Ostmann, N. Krumbholz, D. Mittleman, M. Koch, J. Schoebel, and T. Kürner, "Short-range ultra-broadband terahertz communications: Concepts and perspectives," *IEEE Antennas Propagation Mag.*, vol. 49, pp. 24-39, June 2007.

[5] R. Piesiewicz, C. Jansen, D. Mittleman, T. Kleine-Ostmann, M. Koch, and T. Kürner, "Scattering analysis for the modeling of THz communication systems," *IEEE Trans. Antennas Propagation*, vol. 55, pp. 3002-3009, November 2007.

[6] S. Kim and A. Zajic, "Path loss model for 300-GHz wireless channels," *Proc. of IEEE International Symposium on Antennas and Propagation*, pp. 1–2, Memphis, Tennessee, USA, July 2014.

[7] S. Kim and A. Zajic, "Statistical characterization of 300-GHz propagation on a desktop," to appear in *IEEE Transactions on Vehicular Technology*.

[8] Y. Yang, M. Mandehgar, and D. Grischkowsky, "Broadband THz pulse transmission through the atmosphere," *IEEE Transactions on Terahertz Science and Technology*, vol. 1, pp. 264–273, September 2011.

[9] R. Piesiewicz, T. Kleine-Ostmann, N. Krumbholz, D. Mittleman, M. Koch, and T. Kürner, "Terahertz characterisation of building materials," *IEEE Electronic Letters*, vol. 41, pp. 1002-1004, 2005.

[10] C. Jansen, R. Piesiewicz, D. Mittleman, T. Kürner, and M. Koch, "The impact of reflections from stratified building materials on the wave propagation in future indoor terahertz communication systems," *IEEE Trans. Antennas Propagation*, vol. 56, no. 5, pp. 1413–1419, 2008.

[11] S. Priebe, M. Jacob, C. Jastrow, T. Kleine-Ostmann, T. Schrader, and T. Kürner, "A comparison of indoor channel measurements and ray tracing simulations at 300 GHz," *Proc. Int. Conf. Infrared Millim. Terahertz Waves (IRMMW-THz)*, 2010.

[12] J. M. Jornet and I. F. Akyildiz, "Channel modeling and capacity analysis for electromagnetic wireless nanonetworks in the terahertz band," *IEEE Transactions on Wireless Communications*, vol. 10, pp. 3211–3221, October 2011.

[13] D. W. Matolak, S. Kaya, A. Kodi "Channel modeling for wireless networks-on-chips," *IEEE Communications Magazine*, vol. 51, no. 6, pp. 180–186, June 2013.

[14] A. G. Zajić, *Mobile-to-Mobile Wireless Channels*.Artech House, Boston MA, January 2013.